Aircraft Measurements and Numerical Simulations of an Expansion Fan off the California Coast

Thomas R. Parish

Department of Atmospheric Science, University of Wyoming, Laramie, Wyoming

David A. Rahn

Department of Geography and Atmospheric Science, University of Kansas, Lawrence, Kansas

David C. Leon

Department of Atmospheric Science, University of Wyoming, Laramie, Wyoming

(Manuscript received 29 February 2016, in final form 18 May 2016)

ABSTRACT

Mountains along the California coastline play a critical role in the dynamics of marine atmospheric boundary layer (MBL) airflow in the vicinity of the shoreline. Large changes in the MBL topology have been known to occur downwind of points and capes along the western coast of the United States. Large spatial gradients in wind and temperature become established that can cause anomalous electromagnetic wave propagation. Detailed airborne measurements using the University of Wyoming King Air were conducted to study the adjustment of the MBL to the Point Arguello and Point Conception headlands. Pronounced thinning of the MBL consistent with an expansion fan occurred to the south of Point Conception on 13 June 2012. A sharp cloud edge was collocated with the near collapse of the MBL. D-value cross sections derived from differential GPS altitude measurements allow assessment of the vertical profile of the horizontal pressure gradient force and hence thermal wind forcing in response to the near collapse of the MBL. The Weather Research and Forecasting Model was run with a 1-km grid spacing to examine the atmospheric adjustment around Point Conception during this period. Results from the simulations including the vertical cross sections of the horizontal pressure gradient force were consistent with the aircraft observations. Model results suggest that divergence occurs as the flow rounds Point Conception, characteristic of an expansion fan. Wind speeds in the MBL increase coincident with the decrease in MBL thickness, and subsiding flow associated with the near collapse of the MBL is responsible for the sharp cloud edge.

1. Introduction

An extensive body of literature focuses on the summertime marine atmospheric boundary layer (MBL) flows adjacent to the California coast. A low-level northerly wind regime becomes established in response to the cool Pacific high to the west and a thermal low over the continental southwestern United States (e.g., Beardsley et al. 1987; Zemba and Friehe 1987; Burk and Thompson 1996). Given that the MBL is bounded on the east by a nearly continuous coastal mountain chain and vertically capped by a strong subsidence inversion associated with the Pacific high, MBL characteristics have been interpreted by applying hydraulic flow theory (e.g., Dorman 1985; Winant et al. 1988; Samelson 1992).

The points and capes along the western coast of the United States significantly perturb the wind and temperature fields within the MBL adjacent to the shoreline (e.g., Dorman et al. 1999; Haack et al. 2001). The impact of such MBL changes is profound. Strong gradients in boundary layer height and associated wind and temperature fields emerge. Such conditions can lead to anomalous propagation of electromagnetic signals. Horizontal ducting that impacts microwave transmission can occur (e.g., Haack and Burk 2001). Although some modeling efforts have been conducted (Burk and Thompson 1997; Haack and Burk 2001), few observations have been conducted of the adjustment of the marine layer to the coastal terrain and of the pronounced MBL changes downwind of headlands.
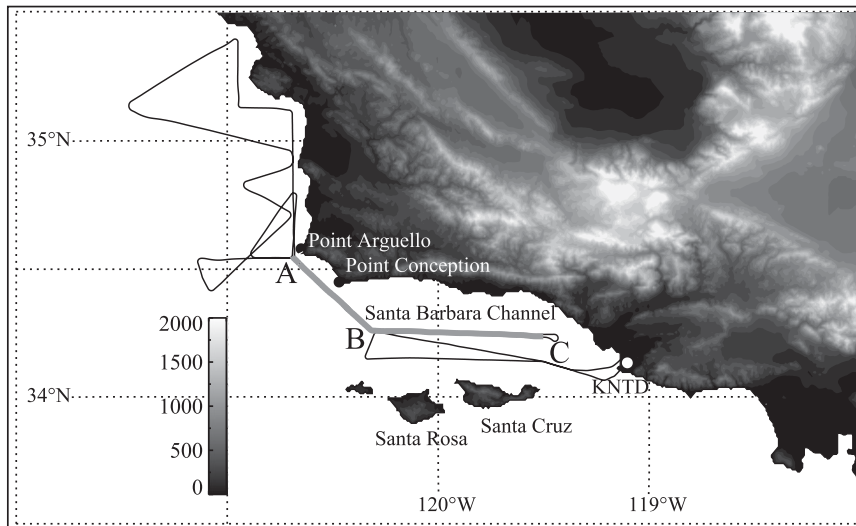
FIG. 1. UWKA flight track (thin, solid lines) for the 13 Jun 2012 case and select geographical features. Thick gray lines (ABC) indicate the path of vertical sawtooth legs. Terrain elevations (m) are in gray shading, with the scale indicated.

Koračin and Dorman (2001) note that major points and capes along the California coast (see Fig. 1 for geographic details) have a local maximum in mean monthly wind speed downwind based on results from a monthlong series of model simulations. Point Conception is situated at the most pronounced bend in the California coastline. Dorman and Koračin (2008) have noted that mean conditions support a MBL compression bulge upwind of Point Conception with an expansion fan downwind as the flow moves around the bend in the coastline and into the Santa Barbara Channel (see also Rahn et al. 2014).

Here, the dynamics associated with pronounced MBL changes near Point Conception are examined using observations from a research aircraft and a finescale numerical simulation for the case of 13 June 2012. It was observed that a near collapse of the MBL occurred in response to relatively strong northwesterly flow that reaches the bend in the coastline near Point Conception. The unique airborne observations of the horizontal pressure field and thermal wind forcing arising at the point of collapse are presented. The numerical simulations are compared with the observations to assess model performance and to provide the broader context within which the aircraft observations were made. Results are summarized in section 4.

2. Observations of an expansion fan near Point Conception

a. Overview

The Precision Atmospheric Marine Boundary Layer Experiment (PreAMBLE) field campaign was conducted during May–June 2012 with a base at Point Mugu, California (KNTD in Fig. 1). Data collected by the University of Wyoming King Air research aircraft (UWKA) form the primary observational basis of this study. Aside from airborne measurements of the basic state variables of wind and temperature, key measurements include accurate static pressure (Rodi and Leon 2012) and precise aircraft altitude based on differential GPS (Parish and Leon 2013). Such measurements allow the horizontal pressure gradient force to be evaluated and hence the ageostrophic nature of the wind field can be explored. Without determining the horizontal pressure gradient force, examining just the wind field would merely be a kinematic study. This is what separates PreAMBLE from previous observational studies of the MBL.

Two flight leg strategies were used during PreAMBLE: isobaric legs and vertical sawtooth patterns. Isobaric legs allow direct measurement of the height of the isobaric surface, the gradient of which is proportional to the horizontal pressure gradient force. Vertical sawtooth patterns, consisting of repeated ascents and descents, enable mapping of the vertical profiles of potential temperature and winds. Differential-GPS-based aircraft altitude measurements enable assessment of D-values from the vertical sawtooth profiles (Parish et al. 2016). D-values are simply the difference between the actual height above sea level and the height of that pressure surface from the *U.S. Standard Atmosphere* (e.g., Bellamy 1945). The use of D-values in cross sections of the atmosphere effectively removes the vertical component of the pressure gradient force, thereby allowing direct visualization of the
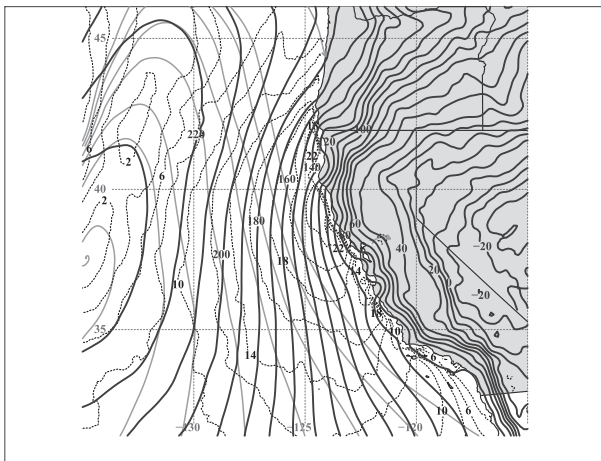
FIG. 2. Large-scale conditions at 0000 UTC 14 Jun 2012, including 1000-hPa height contours (thick lines; m), wind speeds (dotted lines; m s^{-1}), and streamlines (gray solid lines) based on the NCEP 12-km NAM.

horizontal pressure gradient (e.g., Fig. 13 in Bellamy 1945). Because cross sections of D-values show vertical changes in the horizontal pressure gradient force, they also illustrate the thermal wind.

During PreAMBLE, the UWKA carried upward- and downward-looking versions of the Wyoming Cloud Lidar (WCL). The WCLs operate at 355 nm and are designed for retrieval of cloud and aerosol properties and are well suited for determination of cloud boundaries and detection of the MBL top. The returned signal for the upward-looking lidar is sampled at 3.75 m while the signal for the downward-looking lidar is sampled at 1.5-m intervals. Details regarding the lidars can be found in Wang et al. (2009) and Wang et al. (2012). The lidar data are typically combined with the inertial navigation system/GPS data from the King Air to produce time–height cross sections of the attenuated backscatter and depolarization ratio (both uncalibrated). (For a complete list of UWKA instruments, resolutions, and accuracies, see http://www.atmos.uwyo.edu/uwka/users/capabilities.shtml.)

The UWKA flight on 13–14 June 2012 (see Fig. 1 for flight path) focused on the nearshore MBL in the vicinity of the extreme bend of coastal topography encompassing the Point Arguello and Point Conception headlands. Vertical sawtooth legs were directed along the Santa Barbara Channel (from C to B in Fig. 1), followed by an additional vertical sawtooth leg along the coastal topography near Point Conception and Point Arguello (from B to A in Fig. 1). Such patterns were conducted during the initial phase of the flight from 2208 to 2247 UTC and again in reverse (from A to B to C) about 2 h later.

Figure 2 shows the 1000-hPa height contours and wind speeds at 0000 UTC 14 June from the NCEP operational

12-km North American Mesoscale Forecast System (NAM). A strong horizontal pressure gradient was present normal to the coastline that supported coast-parallel winds. The strongest winds were found south of Cape Mendocino within about 100 km of the coast, consistent with the tightest isobaric height gradients that occurred along this stretch. Significant local acceleration of the wind by coastal terrain irregularities, similar to that described in Dorman and Koračin (2008), was apparent with a wind maximum situated just south of Cape Mendocino. Farther south along the coast, the wind speeds decreased. At buoy 46054 (near point B in Fig. 1) the wind speed was 10 m s^{-1}, higher than the mean 7-m wind speed in June 1999 shown in Dorman and Koračin (2008, cf. their Fig. 1) that is 7 m s^{-1} off Point Conception. Winds at 1000 hPa generally remained parallel to the coast.

Wind speeds from the NAM at this level over the region of interest just to the west of Point Arguello were about 12 m s^{-1}. This case is classified as "strong" using the criteria in Dorman and Koračin (2008). Wind speeds decreased to the east within the Santa Barbara Channel; speeds dropped to less than 6 m s^{-1} at the far eastern end of the channel near Point Mugu. Streamlines were similar to those that can be inferred from the mean June 1999 climatology shown in Dorman and Koračin (2008). Wind directions adjacent to the coastline near Point Arguello and Point Conception became more westerly as the flow neared the Santa Barbara Channel, similar to the wind vectors shown in Fig. 1 of Dorman and Koračin (2008).

Satellite imagery from 13 June 2012 (Fig. 3) shows extensive low clouds to the west of the Santa Barbara Channel throughout the day. Clouds were also present along the eastern portion of the California Bight including over the far eastern end of the Santa Barbara Channel. Of note is the sharp cloud boundary evident at the western end of the Santa Barbara Channel in Fig. 3. The sharp cloud edge persisted throughout the day and was sampled during the airborne mission. Clear skies prevailed west of Santa Cruz Island to just south of Point Conception.

b. UWKA measurements

The UWKA conducted a mission between 2110 UTC 13 June 2012 and 0050 UTC on 14 June 2012. Vertical sawtooth legs were flown by climbing and descending between approximately 150 and 900 m above the ocean while maintaining a fixed heading. This study focuses on the series of vertical sawtooth maneuvers adjacent to the headlands of Point Arguello and Point Conception that were conducted to examine the pronounced changes in the depth of the MBL and the
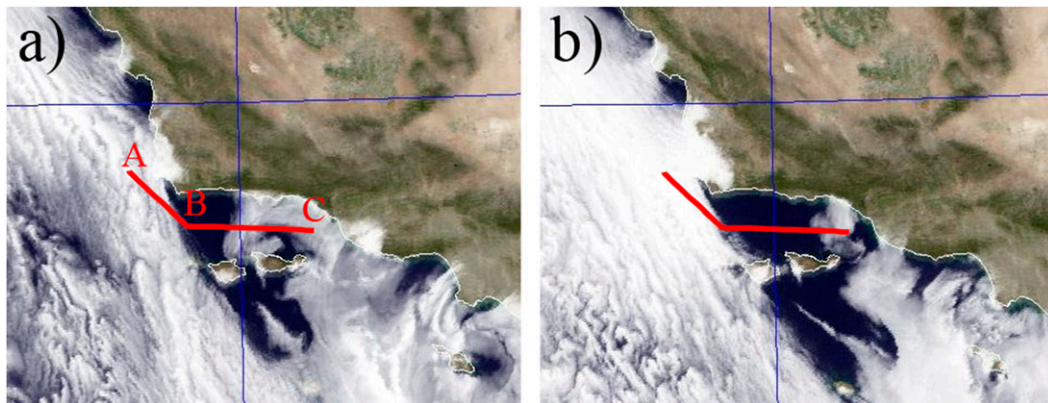
FIG. 3. GOES-West visible imagery from the Naval Research Laboratory at (a) 2200 UTC 13 Jun 2012 and (b) 0000 UTC 14 Jun 2012. The thick red line indicates the UWKA flight track with reference points as in Fig. 1.

associated changes of flow within the MBL. A similar feature was noted on previous flights (e.g., Rahn et al. 2014; Parish et al. 2014) that provided incentive for the flight maneuvers conducted on this day.

Figure 4 depicts potential temperatures and wind speeds along a cross section between points A and C in the flight track shown in Fig. 1. A near collapse of the MBL is evident at about 2200 UTC (Fig. 4a) from the steep slope of the isentropes suggesting that the MBL height decreases from approximately 600 m to less than 200 m over a distance of 50 km. The general structure of the isentropes and wind speeds does not change much in the subsequent 2 h with the strong gradient of MBL height remaining apparent on the return vertical sawtooth (Fig. 4b) and its position also persists.

Dorman and Koračin (2008), among others, point out that hydraulic effects can become apparent if the upstream MBL is supercritical (Froude number greater than 1.0). A supercritical layer exists when the speed of the flow within the MBL is greater than the speed of the fastest possible gravity wave within the layer, thus gravity waves cannot propagate upstream. Hydraulic features can also happen under transcritical conditions (Froude number between 0.5 and 1.0) as shown by Rogerson (1999). A transcritical layer exists when a subcritical layer transitions into a supercritical layer in the vicinity of coastal bends. The Froude number is defined as $\mathrm{Fr} = U/\sqrt{g(\Delta\theta/\theta)h}$, where U is the mean flow in the MBL, h is the MBL depth, g is the acceleration due to gravity, $\Delta\theta$ represents the change in potential temperature across the MBL inversion, and θ is the mean potential temperature within the MBL.

An estimate of the Froude number can be obtained from the sawtooth profiles shown in Fig. 4. The mean MBL wind speed at the western edge of the vertical sawtooth pattern upstream from the MBL collapse

(Fig. 4) is about $10\,\mathrm{m\,s^{-1}}$, the MBL height is 600 m, and the potential temperature difference across the top of the MBL is 7 K. This yields a Froude number about 0.8, providing evidence that the flow is transcritical upstream of the western edge of the cross section at point A in Fig. 1. As the MBL height decreases, wind speeds
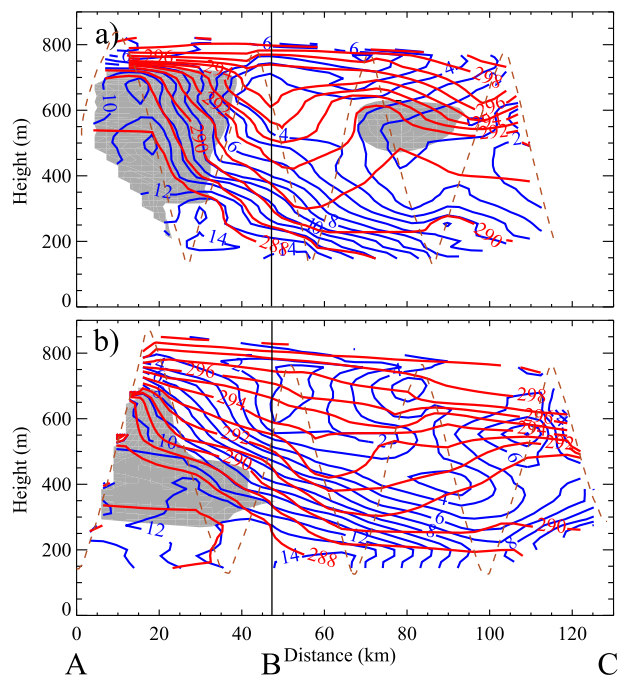

FIG. 4. King Air measurements obtained during vertical sawtooth profiles along leg ABC in Fig. 1 (a) between 2208 and 2234 UTC 13 Jun 2012 and (b) between 0011 and 0035 UTC 14 Jun 2012 showing potential temperatures (red; K) and wind speeds (blue; m s^{-1}). Shading indicates regions of cloud as determined from liquid water contents in excess of 0.5 g kg^{-1}. The flight track is indicated by brown dashed lines. The vertical black line indicates point B in Fig. 1 where the aircraft heading changed. Northwest is to the left.
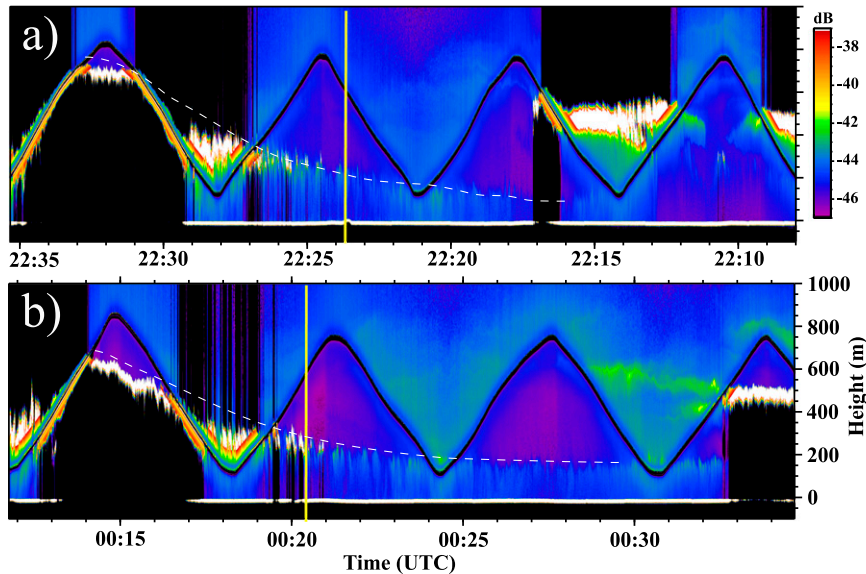
FIG. 5. Copolarized power (dB, uncalibrated) from upward- and downward-pointing Wyoming Cloud Lidar during period of vertical sawtooth maneuvers shown in Fig. 4 along leg ABC for (a) 2208–2234 UTC 13 Jun 2012 and (b) 0011–0035 UTC 14 Jun 2012. West is to the left in both panels. The vertical yellow line indicates point B in the UWKA track shown in Fig. 1, representing the time of the heading change. The dashed white line is an estimate of MBL height.

increase as shown by cross sections in Fig. 4. Taking the MBL height to be 200 m downstream of the near collapse and a wind speed of 14 m s^{-1} and keeping the potential temperature difference at 7 K, the Froude number increases to 2.0. Relaxing the wind speed to 12 m s^{-1} still yields a Froude number well in excess of 1.0, confirming that the flow must be supercritical following the MBL height change.

Although determination of the Froude number based on observations is inherently subjective and imprecise in the real atmosphere (Burk and Thompson 1996), we conclude that the flows shown in Fig. 4 represent a transition from transcritical to supercritical. Observations are also consistent with an expansion fan. Note that isotachs in both cross sections follow isentropes and wind speeds increase monotonically as the MBL thins. Maximum wind speeds of 14 m s^{-1} occur where the MBL thickness reaches a minimum.

A sharp cloud boundary along the western end of the Santa Barbara Channel revealed in visible satellite imagery (Fig. 3) was also observed from the UWKA during this mission. Aircraft measurements of liquid water content (Fig. 4a) indicate that the cloud boundary is collocated with the steep descent of the isotachs and isentropes, showing that the near collapse of the MBL is linked to the sharp cloud edge. Given that the overall MBL height pattern in Fig. 4 changes minimally over the ~2 h elapsed between the cross sections shown in

Figs. 4a and 4b, it is not surprising that the cloud edge visible in Fig. 3 does not change significantly.

Information regarding the near collapse of the MBL can also be obtained from returns from the WCL. Figure 5 illustrates the attenuated backscatter from both upward- and downward-pointing lidars along the sawtooth profiles obtained along legs ABC on outgoing (Fig. 5a) and incoming (Fig. 5b) legs. The WCL became an important measurement tool during PreAMBLE since the aerosol loading in the lower atmosphere over the ocean enabled detection of subtle layering. WCL backscatter in Fig. 5 shows the sharp decrease in the MBL height between 2226 and 2232 UTC (Fig. 5a) and between 0015 and 0020 UTC (Fig. 5b) that matches the collapse of the MBL shown by the isentrope pattern in Fig. 4.

Clouds are evident in Fig. 5 on both the western (left) and eastern (right) ends of the leg, showing up in the WCL images as areas of high backscatter (white). The lidar cannot penetrate deep into the cloud since the power is quickly attenuated by the cloud droplets. Clouds on the left side of the image disappear as the MBL height is reduced to below the lifting condensation level. Convective plumes, visible as regions of higher attenuated backscatter near point B, are still evident because of their higher humidity and aerosol content relative to the overlying air and are used to identify the top of the MBL. Clouds are also evident toward the eastern end of
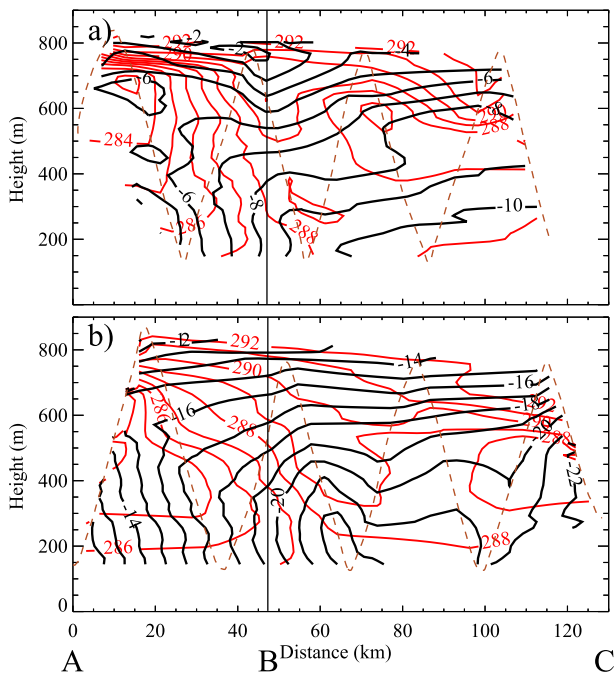
FIG. 6. As in Fig. 4, but for D-values (black; m) and temperatures (red; K).

the Santa Barbara Channel near the right side of the figure, which is consistent with the visible satellite imagery (Fig. 3).

Depolarization signals have been used to provide a means of detecting aerosol source regions during PreAMBLE (e.g., Parish et al. 2014). High values of depolarization ratio suggests scattering from irregularly shaped particles such as dust or other dry aerosol typically associated with a continental source region. In the MBL, deliquesced aerosols prevail. They are inherently spherical and therefore correspond to a lower depolarization ratio. Sawtooth profiles shown in Fig. 5 had rather low depolarization ratios throughout the respective legs (not shown) that suggest that the aerosols are likely of marine origin. No pronounced offshore flow can be documented that accompanies the MBL collapse in this case.

Figure 6 illustrates the resulting D-values and temperatures from the vertical sawtooth profiles. Both the initial pass (2208–2234 UTC; Fig. 6a) and final sawtooth (0011–0035 UTC 14 June; Fig. 6b) show that the strongest horizontal gradients in D-values are found near the lowest level of the sawtooth on the western side of the domain. It follows that the horizontal pressure gradient force decreases rapidly to the east in the lowest 400 m between points A and B in both Figs. 6a and 6b and is especially pronounced in Fig. 6b. Analyses are complicated somewhat by the change in heading at point B in

Fig. 1 (marked by vertical bars in Fig. 6). Notwithstanding the change in track, D-values point to a strong acceleration directed to the east since D-values decrease sharply between point A and slightly past point B. The D-value cross section shown in Fig. 6b indicates a large low-level horizontal pressure gradient associated with the MBL collapse of approximately 10 m per 60 km in the lowest few hundred meters of the atmosphere. This D-value gradient corresponds to a geostrophic wind magnitude of $20\,m\,s^{-1}$. The highest wind speed in the cross section is $14\,m\,s^{-1}$.

Given the sloping isotherms that accompany the pronounced MBL height decrease, a strong thermal wind is present. This is most apparent in Fig. 4b. For example, note the strong gradient in potential temperature near point B along the track near the 47-km mark at a height between about 200 and 600 m. With cooler air to the west, a southerly thermal wind exists that opposes the northerly geostrophic wind. The impact of the thermal wind is that the geostrophic wind component normal to the cross section must decrease with height. Since the normal component of the geostrophic wind is proportional to the isobaric slope of D-values, the thermal wind must manifest as a decrease of the isobaric D-value slopes with height. Note that pronounced changes in the D-value slopes are present above 200 m at point B. The decreasing slopes continue with height at point B until about 800 m where D-values become oriented nearly horizontal, implying that the normal component of the geostrophic wind is approaching zero.

It can be seen from both Figs. 6a and 6b that the orientation of D-value contours changes dramatically in response to the sloping isotherms at point B that mark the near collapse of the MBL. Analyses shown in Fig. 4 illustrate the strong link between the sloping isotherms and D-values. Given that measurements of temperature and D-values are determined independently, the obvious link as shown in Fig. 4 demonstrates the ability of the UWKA to determine D-values and provides evidence as to the validity of the analyses.

From measurements shown in Fig. 6, it is appropriate to examine the thermal wind balance associated with the MBL adjustment. To address the thermal wind issue, we focus on the returning sawtooth (Fig. 6b) and consider only the first ~50 km of the leg between points AB when the plane flew at a heading of 128°, nearly along the axis of the wind. For the entire sawtooth maneuver, the resultant wind was $8.5\,m\,s^{-1}$ from 317°. From the cross section, the cross-leg geostrophic wind at each level is obtained from the interpolated horizontal height gradient. In addition, if it is assumed that the geostrophic wind is known at the lowest level, the geostrophic wind at upper levels can be determined by adding the thermal
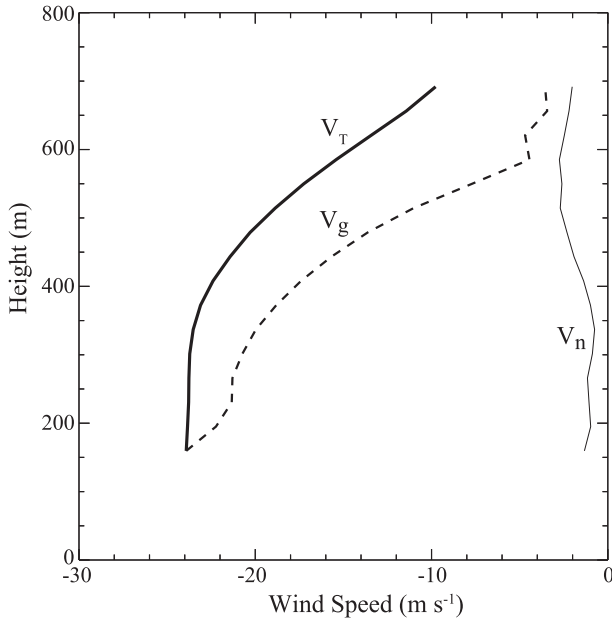
FIG. 7. Interpolated values of the geostrophic wind inferred from the thermal wind (black solid line; m s^{-1}), actual measured geostrophic wind (black dashed line; m s^{-1}), and normal component of the wind along vertical sawtooth leg AB in Fig. 1 from 0011 to 0021 UTC 14 Jun 2012.

FIG. 8. WRF-simulated stratus (gray shading), 990-hPa heights (black solid lines; m), wind speeds (blue solid lines; m s^{-1}), 990-hPa streamlines (dark-red solid lines), and temperatures (red dashed lines; °C) at 0000 UTC 14 Jun 2012. The thick black line depicts the UWKA vertical sawtooth track between 0011 and 0034 UTC.

wind. Integrating the thermal wind at successive levels provides an estimate of the geostrophic wind.

Figure 7 illustrates the relationship between the geostrophic wind profile as determined from the D-value slopes and the geostrophic wind as estimated from the thermal wind relationship. While there is an offset between the measured and inferred geostrophic wind obtained from thermal wind constraints, the general shape is the same for each case. Since the winds are directed along the flight track, the wind components normal to the flight leg are thus highly ageostrophic in the vicinity of the MBL collapse. Largest normal ageostrophic wind components of about 22 m s^{-1} are found at the lowest levels; strong downgradient acceleration is present along the flight path as the MBL collapses.

3. WRF simulation of the 13 June 2013 case

Version 3.7 of the WRF Model (Skamarock et al. 2008) was used to simulate the 13 June 2012 case. The nesting strategy consists of four domains, with the innermost nest consisting of 211 × 211 grid points with a horizontal grid spacing of 1 km. A total of 84 vertical levels were used with increasing resolution in the lower atmosphere. The model was initialized at 0000 UTC 13 June with the 12-km NAM grids and run for a 30-h period.
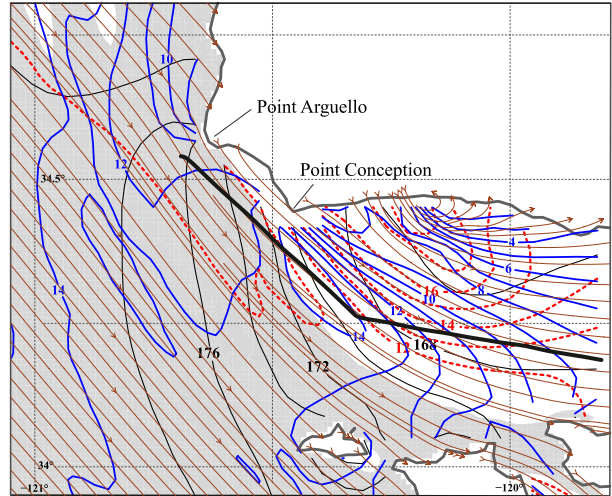
In attempt to generate high-fidelity simulations for PreAMBLE cases to enable comparison with aircraft observations, extensive testing of relevant WRF parameterization schemes was performed. Cases such as 13 June 2012 had characteristic cloud features that were often difficult to match. Key parameterizations used for the run are the following: Lin (Purdue) microphysics scheme, the new Goddard scheme for longwave radiation physics, the Dudhia scheme for shortwave radiation physics, MM5 surface-layer similarity with the unified Noah land surface model, and the Yonsei University boundary layer physics scheme. Here we focus on the innermost nest to compare with the UWKA observations.

Figure 8 illustrates the 990-hPa heights, temperatures, streamlines and wind speeds, and MBL cloud coverage at 0000 UTC 14 June. This period corresponds to the time at which the UWKA was completing vertical sawtooth legs during the return portion of the flight. The level is roughly at the lowest point of the vertical sawtooth legs (e.g., Figs. 4b, 6b). The outstanding feature in this simulation is the sharp cloud edge that matches well with that observed in the satellite imagery shown in Fig. 2b. Cloud extent simulated in WRF also matches well with the observed cloud features.

As in the UWKA observations, winds are predominantly from the northwest over the western Santa Barbara Channel. Wind speeds reach a maximum of 14 m s^{-1} south of Point Conception. This corresponds well with the wind speeds in the lower portion of the vertical sawtooth pattern in Fig. 4b. Wind speeds
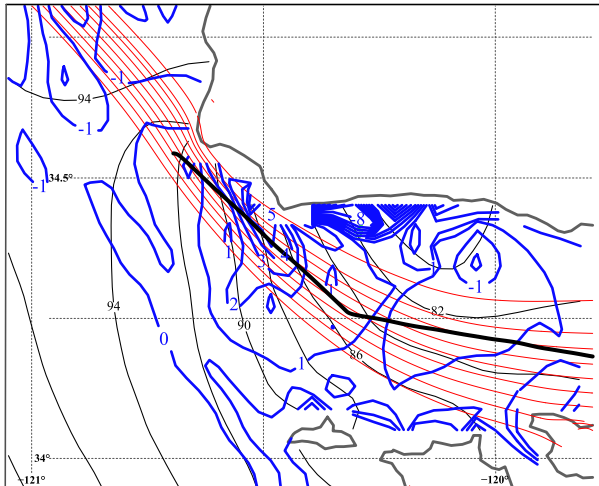
FIG. 9. WRF-simulated 1000-hPa heights (black solid lines; m), select 1000-hPa streamlines (red solid lines), and horizontal divergence (blue solid lines; $\times 10^{-4}\,\mathrm{s}^{-1}$).
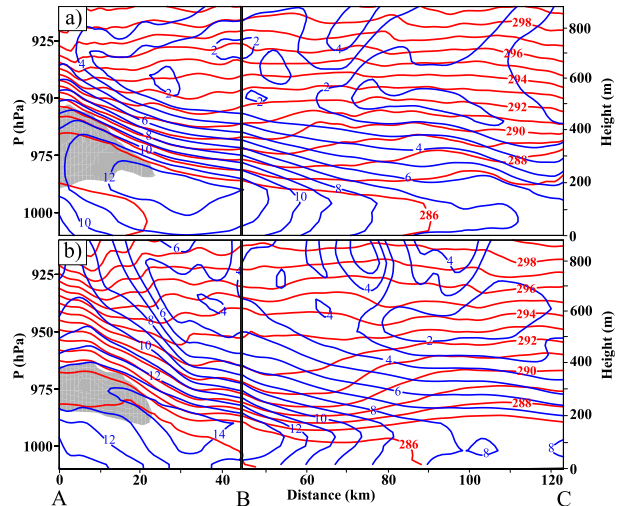

FIG. 10. Results from WRF simulation along track ABC in Fig. 1 at (a) 2200 UTC 13 Jun 2012 and (b) 0000 UTC 14 Jun 2012 showing potential temperatures (red; K) and wind speeds (blue; $\mathrm{m\,s}^{-1}$). The vertical solid line indicates point B in Fig. 1 where the aircraft changed its heading. Northwest is to the left.

at 990 hPa decrease in an eastward direction along the Santa Barbara Channel, again consistent with the observations.

Temperatures at 990 hPa in the WRF simulation at 0000 UTC 14 June 2012 show only minor changes of less than 2 K along the UWKA flight path, in general agreement with the observations at the lowest level of the sawtooth pattern. WRF simulations show extensive low-level offshore flow over the northern section of the Santa Barbara Channel that is responsible for significant warming adjacent to the shore, a feature we were not able to confirm since the flight path outgoing and inbound was too far south.

Given the fidelity of the sharp cloud edge in the WRF simulation and the good agreement with the UWKA observations at the 990-hPa level, it is assumed that the primary physical processes at work are well replicated in the vicinity of the MBL collapse. The WRF simulation provides insight into the development of the expansion fan. Figure 9 shows the 1000-hPa streamlines and divergence field at 0000 UTC 14 June 2012. Streamlines from WRF show a classic diffluence pattern from Point Arguello into the western Santa Barbara Channel. Strong divergence is collocated with the streamline diffluence. The largest divergence is found midway along leg AB in the UWKA sawtooth where the MBL depth rapidly decreases. The large ageostrophic component directed toward the northeast (Fig. 7) implies an acceleration of the flow toward the southeast. Thus, along-track divergence occurs as the flow accelerates. We conclude that the MBL near collapse as seen from the UWKA observations in Figs. 4 and 6 is consistent with an expansion fan as discussed by Dorman and Koračin (2008).

To compare the WRF results with UWKA observations, cross sections (Fig. 10) have been prepared from the model output along the same track (ABC in Fig. 1) for both outbound and inbound sawtooth legs (segments along AB and BC are again differentiated by vertical lines). Isotachs from WRF closely follow isentropes near the top of the boundary layer as the MBL undergoes the sudden height change along leg segment AB between about 975 and 925 hPa for both the outbound (2200 UTC) and inbound (0000 14 June) tracks. Examination of the 286-K isentrope that is used as a proxy for the MBL top shows a decrease from about 350 m at point A to less than 200 m by point B. Wind speeds at the 200-m level show a sharp decrease eastward along the Santa Barbara Channel from a maximum of 14 m s^{-1} near point B to a minimum of about 7 m s^{-1} approaching point C.

The positioning of the steep MBL height decrease as evidenced by the 286-K isentrope between points A and B is collocated with the strongest divergence seen in Fig. 8, again suggesting that the MBL near collapse is the result of the expansion fan. The cloud edge slightly past 20 km in Fig. 10 is situated at the midpoint of the steep decrease of the MBL height. The wind speed magnitude, the pattern of wind decrease with distance, and the isentrope slopes all agree well with UWKA observations in the vicinity of the MBL collapse between point A and the 60-km distance marker as shown in Fig. 4a. Isentrope slopes in Fig. 10 between A and B near the top of the MBL are less steep than those depicted from the UWKA data in Fig. 4. The model solution also departs
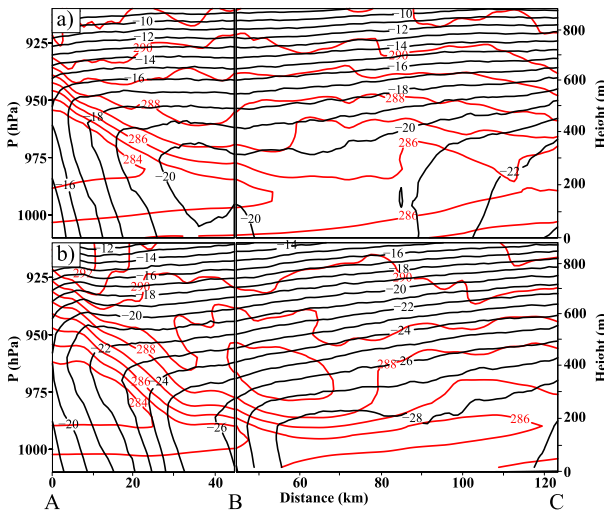
FIG. 11. As in Fig. 10, but for D-values (black; m) and temperatures (red; K).

from observations along the eastern end of leg ABC within the Santa Barbara Channel where the simulation has relatively equally spaced isentropes above 200 m, while the observations suggest more finescale structure. Although the general features near the MBL tend to be well simulated by WRF, the finescale isentrope slopes attendant with the MBL collapse and especially MBL height has presented a challenge for this and other case studies (e.g., Rahn et al. 2014).

Dynamics of the MBL near collapse can be seen in the cross section of D-values and temperatures from the WRF simulation at 2200 UTC 13 June (Fig. 11a) and 0000 UTC 14 June 2012 (Fig. 11b). In each case, the near collapse of the MBL is pronounced and indicated by the sloping isotherms. The top of the MBL is marked by an inflection in the D-values, consistent with the thermal wind forcing. The horizontal pressure gradient force undergoes a pronounced decrease with height as a result of the horizontal temperature gradients such that the geostrophic winds along section AB at 0000 UTC 14 June 2012 shift from about $20 \, \text{m s}^{-1}$ at the surface to near zero above 930 hPa. D-values from WRF are consistent with those measured from the UWKA platform (Fig. 6) and show the strong decrease in the horizontal pressure gradient force in response to the near collapse of the MBL.

4. Conclusions

Aircraft observations and high-resolution numerical simulations from WRF demonstrate that a large MBL adjustment is present south of Point Conception during 13 June 2012. A sharp cloud boundary forms at the point marking the MBL collapse that was observed from the

UWKA platform and simulated in WRF. Aircraft observations suggest that the MBL flow was transcritical around the Point Arguello and Point Conception headlands. A near collapse of the MBL is observed, consistent with an expansion fan (e.g., Dorman and Koračin 2008). Aircraft observations taken just downwind from Point Conception show supercritical conditions with acceleration occurring as the MBL thins.

Vertical sawtooth flight tracks were made across the expansion fan to capture the dynamics and thermodynamics of the near collapse. A strong horizontal pressure gradient was present at the lowest level of the flight track about 150 m above the ocean surface that supports a geostrophic wind component of approximately $20 \, \text{m s}^{-1}$ normal to the cross section along the zone of strongest MBL height change between points A and B. Since the actual winds measured by the UWKA were from 317°, nearly along the axis of the flight track, a large ageostrophic component is present. The ageostrophic component normal to the cross-section line AB was larger than $20 \, \text{m s}^{-1}$ at levels between 200 and 400 m.

Strong horizontal temperature gradients are present with the expansion fan. New airborne capabilities permit direct assessment of the vertical profile of the horizontal pressure gradient force from the sawtooth patterns. These observations show that the thermal wind opposes the geostrophic wind normal to the flight track and hence the horizontal pressure gradient force decreases significantly with height. Estimates show that the measured change in the geostrophic wind is roughly that expected from thermal wind considerations. The track-normal horizontal pressure gradient approaches zero above the MBL.

Numerical simulations show that the dynamics of the flow match the aircraft observations. In particular, the thermal wind forcing associated with the MBL collapse is similar to the UWKA observations including the cross sections of D-values. Such a numerical simulation provides the large-scale context for the aircraft observations. Diffluent streamlines at 1000-hPa result in the low-level divergence that we propose is the key forcing mechanism for the observed expansion fan. The intensity of the collapse as measured by the slope of isentropes is slightly weaker in WRF than that actually observed even using the 1-km horizontal resolution domain. Similar to results from previous work (e.g., Rahn et al. 2014), WRF results tend to smooth sharp gradients such as found at the top of the MBL and also associated with the collapse here. This should be recognized when interpreting results of numerical simulations on related topics such as electromagnetic propagation characteristics and ducting.

REFERENCES

Beardsley, R. C., C. E. Dorman, C. A. Friehe, L. K. Rosenfeld, and C. D. Winant, 1987: Local atmospheric forcing during the Coastal Ocean Dynamics Experiment: 1. A description of the marine boundary layer and atmospheric conditions over a northern California upwelling region. *J. Geophys. Res.*, **92**, 1467–1488, doi:10.1029/JC092iC02p01467.

Bellamy, J. C., 1945: The use of pressure altitude and altimeter corrections in meteorology. *J. Meteor.*, **2**, 1–78, doi:10.1175/1520-0469(1945)002<0001:TUOPAA>2.0.CO;2.

Burk, S. D., and W. T. Thompson, 1996: The summertime low-level jet and marine boundary layer structure along the California coast. *Mon. Wea. Rev.*, **124**, 668–686, doi:10.1175/1520-0493(1996)124<0668:TSLLJA>2.0.CO;2.

——, and ——, 1997: Mesoscale modeling of summertime refractive conditions in the Southern California Bight. *J. Appl. Meteor.*, **36**, 22–31, doi:10.1175/1520-0450(1997)036<0022:MMOSRC>2.0.CO;2.

Dorman, C. E., 1985: Evidence of Kelvin waves in California's marine layer and related eddy generation. *Mon. Wea. Rev.*, **113**, 827–839, doi:10.1175/1520-0493(1985)113<0827:EOKWIC>2.0.CO;2.

——, and D. Koračin, 2008: Response of the summer marine layer flow to an extreme California coastal bend. *Mon. Wea. Rev.*, **136**, 2894–2922, doi:10.1175/2007MWR2336.1.

——, D. P. Rogers, W. Nuss, and W. T. Thompson, 1999: Adjustment of the summer marine boundary layer around Point Sur, California. *Mon. Wea. Rev.*, **127**, 2143–2159, doi:10.1175/1520-0493(1999)127<2143:AOTSMB>2.0.CO;2.

Haack, T., and S. D. Burk, 2001: Summertime marine refractivity conditions along coastal California. *J. Appl. Meteor.*, **40**, 673–687, doi:10.1175/1520-0450(2001)040<0673:SMRCAC>2.0.CO;2.

——, ——, C. Dorman, and D. Rodgers, 2001: Supercritical flow interaction within the Cape Blanco–Cape Mendocino orographic complex. *Mon. Wea. Rev.*, **129**, 688–708, doi:10.1175/1520-0493(2001)129<0688:SFIWTC>2.0.CO;2.

Koračin, D., and C. E. Dorman, 2001: Marine atmospheric boundary divergence and clouds along California in June 1996. *Mon. Wea. Rev.*, **129**, 2040–2056, doi:10.1175/1520-0493(2001)129<2040:MABLDA>2.0.CO;2.

Parish, T. R., and D. Leon, 2013: Measurement of cloud perturbation pressures using an instrumented aircraft. *J. Atmos. Oceanic Technol.*, **30**, 215–229, doi:10.1175/JTECH-D-12-00011.1.

——, D. A. Rahn, and D. Leon, 2014: Aircraft observations of the marine layer adjustment near Point Arguello, California. *J. Appl. Meteor. Climatol.*, **53**, 970–989, doi:10.1175/JAMC-D-13-0164.1.

——, ——, and ——, 2016: Research aircraft determination of D-value cross sections. *J. Atmos. Oceanic Technol.*, **33**, 391–396, doi:10.1175/JTECH-D-15-0173.1.

Rahn, D. A., T. R. Parish, and D. Leon, 2014: Coastal jet transition adjustment near Point Conception, California, with opposing wind in the bight. *Mon. Wea. Rev.*, **142**, 1344–1360, doi:10.1175/MWR-D-13-00177.1.

Rodi, A. R., and D. C. Leon, 2012: Correction of static pressure on a research aircraft in accelerated flight using differential pressure measurements. *Atmos. Meas. Tech.*, **5**, 2569–2579, doi:10.5194/amt-5-2569-2012.

Rogerson, A. M., 1999: Transcritical flows in the coastal marine atmospheric boundary layer. *J. Atmos. Sci.*, **56**, 2761–2779, doi:10.1175/1520-0469(1999)056<2761:TFITCM>2.0.CO;2.

Samelson, R. M., 1992: Supercritical marine-layer flow along a smoothly varying coastline. *J. Atmos. Sci.*, **49**, 1571–1584, doi:10.1175/1520-0469(1992)049<1571:SMLFAA>2.0.CO;2.

Skamarock, W. C., and Coauthors, 2008: A description of the Advanced Research WRF version 3. NCAR Tech. Note NCAR/TN-475+STR, 113 pp., doi:10.5065/D68S4MVH.

Wang, Z., P. Wechsler, W. Kuestner, J. French, A. R. Rodi, B. Glover, M. Burkhart, and D. Lukens, 2009: Wyoming Cloud Lidar: Instrument description and applications. *Opt. Express*, **17**, 13 576–13 587, doi:10.1364/OE.17.013576.

——, J. French, G. Vali, and P. Wechsler, 2012: Single aircraft integration of remote sensing and in situ sampling for the study of cloud microphysics and dynamics. *Bull. Amer. Meteor. Soc.*, **93**, 653–668, doi:10.1175/BAMS-D-11-00044.1.

Winant, C. D., C. E. Dorman, C. A. Friehe, and R. C. Beardsley, 1988: The marine boundary layer off northern California: An example of supercritical channel flow. *J. Atmos. Sci.*, **45**, 3588–3605, doi:10.1175/1520-0469(1988)045<3588:TMLONC>2.0.CO;2.

Zemba, J., and C. A. Friehe, 1987: The marine boundary layer jet in the Coastal Ocean Dynamics Experiment. *J. Geophys. Res.*, **92**, 1489–1496, doi:10.1029/JC092iC02p01489.